Geophysical Prospecting, 2006, **54**, 575–587

Anisotropic migration velocity analysis: Application to a data set from West Africa

Debashish Sarkar[1,2]* and Ilya Tsvankin[1]

[1]*Center for Wave Phenomena, Department of Geophysics, Colorado School of Mines, Golden, CO 80401-1887, USA, and* [2]*Now at: GX Technology, 5847 San Felipe, Houston, TX 77057, USA*

Received September 2004, revision accepted March 2006

ABSTRACT

Although it is widely recognized that anisotropy can have a significant influence on the focusing and positioning of migrated reflection events, conventional depth imaging methods still operate with isotropic velocity fields. Here, we present an application of a 2D migration velocity analysis (MVA) algorithm, designed for factorized $v(x, z)$ VTI (transversely isotropic with a vertical symmetry axis) media, to an offshore data set from West Africa. By approximating the subsurface with factorized VTI blocks, it is possible to decouple the spatial variations in the vertical velocity from the anisotropic parameters with minimal *a priori* information.

Since our method accounts for lateral velocity variation, it produces more accurate estimates of the anisotropic parameters than those previously obtained with time-domain techniques. The values of the anellipticity parameter η found for the massive shales exceed 0.2, which confirms that ignoring anisotropy in the study area can lead to substantial imaging distortions, such as mis-stacking and mispositioning of dipping events. While some of these distortions can be removed by using anisotropic time processing, further marked improvement in image quality is achieved by prestack depth migration with the estimated factorized VTI model. In particular, many fault planes, including antithetic faults in the shallow part of the section, are better focused by the anisotropic depth-migration algorithm and appear more continuous. Anisotropic depth migration facilitates structural interpretation by eliminating false dips at the bottom of the section and improving the images of a number of gently dipping features.

One of the main difficulties in anisotropic MVA is the need to use *a priori* information for constraining the vertical velocity. In this case study, we successfully reconstructed the time–depth curve from reflection data by assuming that the vertical velocity is a continuous function of depth and estimating the vertical and lateral velocity gradients in each factorized block. If the subsurface contains strong boundaries with jumps in velocity, knowledge of the vertical velocity at a single point in a layer is sufficient for our algorithm to determine all relevant layer parameters.

INTRODUCTION

Since most subsurface formations are both heterogeneous and anisotropic, building physically realistic velocity models from reflection data remains a highly challenging problem. Conventional velocity-analysis methods, which range from those employing simple analytic functions (e.g. Faust 1953; Gardner *et al.* 1974) to sophisticated tomographic schemes (e.g. Stork 1992; Liu 1997; Meng 1999; Chauris and Noble 2001), are designed to account for smooth spatial velocity

*E-mail: dsarkar@gxt.com

variations but still ignore anisotropy. Their application often causes anisotropy-induced mis-ties in time–depth conversion, undercorrection of non-hyperbolic moveout and misfocusing of dipping events (Tsvankin 2001). In contrast, most existing anisotropic parameter-estimation techniques (e.g. Alkhalifah and Tsvankin 1995; Alkhalifah 1996, 1997; Han *et al.* 2000; Grechka *et al.* 2002) do not properly handle lateral heterogeneity.

Migration algorithms suitable for imaging data from heterogeneous media of relatively simple symmetry (e.g. transversely isotropic) are readily available today. Therefore, the main difficulty is not in the imaging step, but in reconstructing a sufficiently accurate spatially varying, anisotropic velocity field. Non-uniqueness in velocity analysis arises from the trade-offs between the velocity gradients, shapes of the reflecting interfaces, and anisotropic parameters. Some of these trade-offs, such as those between the velocity field and reflector shapes, cannot be resolved without *a priori* information, even for isotropic media (Stork 1988).

In particular, velocity analysis in heterogeneous, anisotropic media is compounded by the interplay between anisotropy and spatial velocity variations. For example, reflection traveltimes from a diffractor in a vertically heterogeneous isotropic medium are fully equivalent to the traveltimes from a diffractor in a homogeneous transversely isotropic medium with a vertical axis of symmetry (VTI). Therefore, it is critically important to represent the subsurface with the simplest possible model that

1 allows for anisotropy and adequately describes realistic velocity variations,

2 permits full understanding of the inherent ambiguities,

3 requires minimal *a priori* information to resolve the relevant parameters.

Such a model for P-wave depth imaging in the presence of transverse isotropy was suggested by Sarkar and Tsvankin (2003) (hereafter referred to as Paper I) who approximated the subsurface by a piecewise-factorized $v(x, z)$ VTI medium with constant gradients in the vertical velocity. The Thomsen (1986) anisotropic parameters, ϵ and δ, in each factorized block or layer are constant, while the P-wave vertical velocity is described by $V_{P0}(x, z) = V_{P0} + k_x x + k_z z$, where V_{P0} is the velocity at the origin of the coordinate system ($x = 0$, $z = 0$), and k_z and k_x are the vertical and horizontal velocity gradients, respectively. A similar factorized subsurface model was used by Sexton and Williamson (1998) and Williamson *et al.* (1999), but their velocity-updating scheme is designed in the time domain and does not fully address inherent trade-offs between the medium parameters, especially that between anisotropy and heterogeneity.

In addition to being the simplest VTI model with both vertical and lateral velocity variations, the factorized $v(x, z)$ VTI medium also allows for an analytic understanding of the ambiguities in parameter estimation. In Paper I, we showed that P-wave reflection moveout constrains only four combinations of the five medium parameters, V_{P0}, k_x, k_z, ϵ and δ, in each factorized block:

1 the normal-moveout (NMO) velocity at the surface $V_{nmo} = V_{P0}\sqrt{1 + 2\delta}$;

2 the vertical gradient k_z;

3 the combination $\hat{k}_x = k_x\sqrt{1 + 2\delta}$ of the lateral gradient k_x and δ;

4 the Alkhalifah–Tsvankin (1995) anellipticity parameter $\eta \equiv (\epsilon - \delta)/(1 + 2\delta)$.

Estimation of the parameters V_{P0}, k_x, ϵ and δ, requires minimal *a priori* information, such as knowledge of the vertical velocity at a single point in the medium.

Sarkar and Tsvankin (2004) (hereafter referred to as Paper II) proposed a migration velocity analysis (MVA) algorithm to invert for the effective (moveout) parameters, V_{nmo}, k_z, $\hat{k}_x$ and η. To separate the influence of anisotropy from that of vertical heterogeneity in each factorized block, it is necessary to use image gathers along two reflectors sufficiently separated in depth. The residual moveout of events in image gathers is evaluated by a semblance operator (Taner and Koehler 1969) that accounts for the non-hyperbolic (long-spread) moveout needed to constrain the anellipticity parameter η using subhorizontal events. The variance of the migrated depths is then minimized by iteratively solving a system of linear equations for the medium parameters (Liu 1997). The algorithm assumes the velocity V_{P0} to be known at one point in each factorized block and searches for the parameters, k_z, k_x, ϵ and δ.

In Paper II, the MVA algorithm is implemented in the layer-stripping mode, wherein the model is divided into factorized VTI blocks or layers, and the medium parameters are estimated one factorized block at a time. Velocity analysis is performed through an iterative two-step procedure that includes Kirchhoff prestack depth migration followed by an update of the medium parameters. The iterations are stopped when events in image gathers associated with two reflectors in each factorized block are sufficiently flat. As illustrated in the Appendix, the piecewise-factorized model with a linear velocity variation in each block usually provides an adequate approximation for non-linear velocity functions.

Here, the algorithm of Paper II is applied to a data set acquired by Chevron Overseas Petroleum Co. in offshore West Africa. The two seismic lines analysed in this paper were previously processed by Alkhalifah *et al.* (1996) and Alkhalifah (1996, 1997) using time-domain velocity analysis that operates with dip moveout (DMO) as well as with non-hyperbolic moveout of subhorizontal events. Both DMO and non-hyperbolic moveout inversion, described in detail by Tsvankin (2001, chapter 7), detected substantial anisotropy in massive shale formations and estimated the parameter η as a function of the vertical reflection time. Time migration for the reconstructed vertically heterogeneous VTI model succeeded in imaging dipping events (fault planes) that were misfocused by conventional algorithms. Also, the VTI processing improved the images of some gently dipping features by properly correcting for non-hyperbolic moveout.

However, since the previous studies were limited to time-domain processing, they did not account for lateral heterogeneity in either parameter estimation or migration. Application of the factorized $v(x, z)$ model here yields more accurate, laterally varying, anisotropic velocity fields and significantly improved imaging of several important structural features.

A BRIEF OVERVIEW OF THE GEOLOGICAL HISTORY

The geology of the area (offshore Angola) is largely governed by tectonic rifting that occurred around the early Cretaceous. The major tectono-stratigraphic units in the order they were formed are (Brice *et al.* 1982):

1 prerift with gentle tectonism,
2 synrift I with strong tectonism,
3 synrift II with moderate tectonism,
4 post-rift with gentle tectonism,
5 regional subsidence with major tilting.

The available seismic sections contain only the subsidence and post-rift phases schematically shown in Fig. 1.

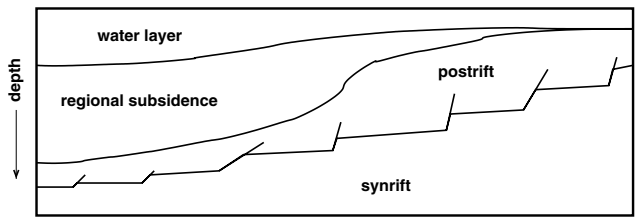

Figure 1 Sketch of the geological history of the area depicting the subsidence, post-rift, and synrift units.

The regional subsidence phase, which dates back to the Oligocene and Miocene times, is characterized by a rapidly deposited regressive sequence, turbidites, shaly clastics and high-pressure shale. Reflectors within this unit are weak and discontinuous, and show extensive cut-and-fill patterns. The ubiquitous presence of shales makes the subsidence unit strongly anisotropic, which is well documented in the literature (Ball 1995; Alkhalifah *et al.* 1996). The thickness of this unit increases away from the shore, and at places can reach 6 km.

The early Tertiary post-rift deposition includes marine clastics and carbonates, non-marine red beds and transgressive sequences. This unit is less anisotropic than the subsidence layer and increases in thickness (up to 2 km) towards the shore. Seismic velocity within the post-rift unit varies significantly and is proportional to the carbonate content in the sediments. The structural style is defined by gentle conformable folds near the top, with faulting and complex halokinesis prevalent at the base.

FIRST LINE

The first section includes primarily subhorizontal interfaces and is about 9 km long. The depth of the water is close to 150 m, and both the subsidence and post-rift units are approximately 2-km thick. Preprocessing steps included dip filtering and muting applied to CMP gathers to remove linear events associated with guided waves; also, amplitudes at late times were boosted by a time-variant gain.

As the first step in building the velocity model, we identified the water bottom by migrating and stacking the data with a moveout velocity of 1500 m/s. Then we estimated the velocity field of the underwater sediments. Because this layer is too thin (≈400 m) to allow for picking of two events sufficiently separated in depth, we were unable to apply our MVA algorithm. Instead, we assumed that the underwater layer is isotropic with water velocity of 1500 m/s at the top and we computed the vertical gradient, $k_z = 0.8\ \mathrm{s}^{-1}$, using NMO velocities obtained from standard semblance velocity analysis. Figure 2 shows common-image gathers after migration with the estimated velocity field in the underwater layer (block II); the bottom of the layer is defined by the deepest events with no residual moveout.

Next, we applied migration velocity analysis to image gathers in block III. To get unique estimates of the medium parameters, we assumed that the vertical velocity V_{P0} is continuous at a certain point on the boundary between the second and the third blocks (see Paper II). Since the residual moveout of events in block III shows insignificant lateral variation

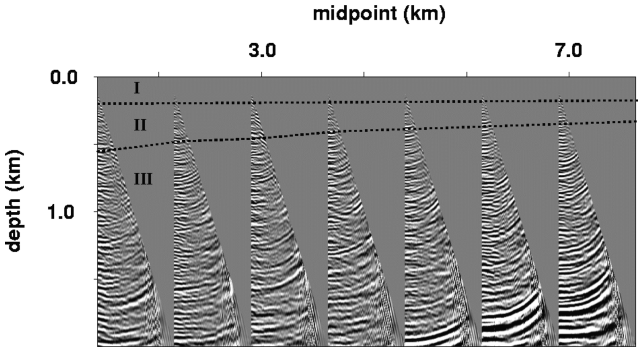

Figure 2 Common-image gathers (computed with an increment of 1 km) after Kirchhoff prestack depth migration with the velocity V_{P0} = 1500 m/s for the water (block I) and the parameters V_{P0} = 1500 m/s and $k_z = 0.8$ s^{-1} for the underwater sediments (block II). Blocks I, II, and III used in the velocity analysis are separated by dashed lines that correspond to the deepest flat events within the first two blocks. The overcorrected events in block III indicate that the velocity field in block II is not appropriate for the deeper reflectors.

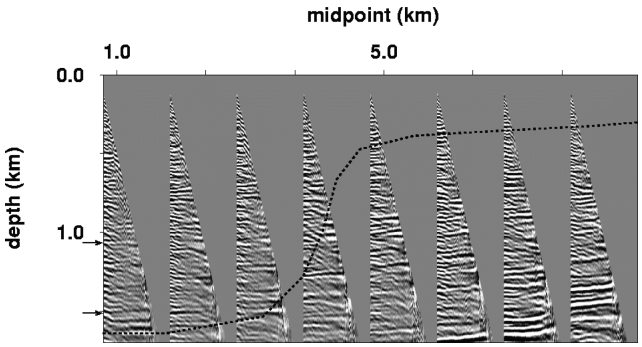

Figure 3 Common-image gathers after migration velocity analysis in block III (above the dashed line). The MVA operated with the two events marked by the arrows for midpoints between 1 km and 3 km. Most events below the dashed line exhibit residual moveout.

(Fig. 2) and the boundary is close to horizontal, we expect that the lateral gradient k_x in this block can be neglected, and any point at the top of block III can be picked as the point of continuity. The velocity was taken to be continuous at the point (x = 3000 m, z = 452 m), which is close to the midpoints where we picked residual moveout and performed the MVA. Computing V_{P0}=1740 m/s at the continuity point and minimizing the residual moveout of two events between midpoints 0 and 3 km (Fig. 3), we estimated the parameters, $k_z = 0.6 \pm 0.03$ s^{-1}, $k_x = 0.0 \pm 0.01$ s^{-1}, $\epsilon = 0.3 \pm 0.03$ and $\delta = 0.06 \pm 0.02$ in block III (see Paper II for a description of the error analysis). Note that the starting model for the MVA algorithm was isotropic and homogeneous.

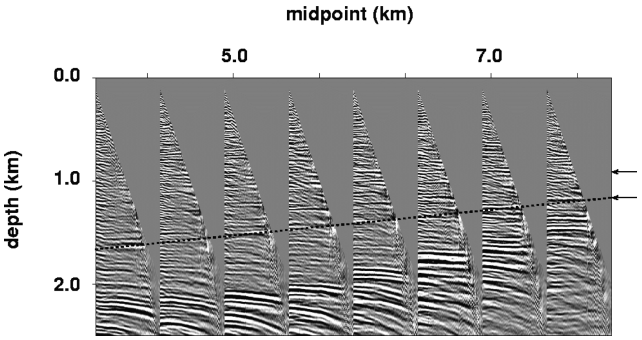

Figure 4 Common-image gathers after migration velocity analysis in block IV using the two events marked by the arrows for midpoints between 6 km and 8 km. The dashed line separates blocks III and IV, where events are practically flat, from the deeper part of the section.

The relatively large values of ϵ and δ, which yield $\eta = 0.21 \pm 0.03$, indicate that this block has pronounced anisotropy. While the inverted parameters remove residual moveout in image gathers at midpoints with coordinates less than 4 km, events in the right-hand part of the section are overcorrected (Fig. 3). Therefore, the third block has a limited lateral extent, as marked in Fig. 3.

The results of MVA for block III indicate the need to introduce another block in the same depth interval but for midpoints to the right of the 4-km mark. Similarly to the procedure described above, we selected the point of continuity between the underwater layer and the new block IV close to the midpoints where we performed the MVA (x = 7000 m, z = 310 m) and computed the vertical velocity at this point (V_{P0} = 1625 m/s). Keeping this value of V_{P0} fixed, we carried out the migration velocity analysis using the residual moveout of the two events marked in Fig. 4 between midpoints 6 km and 8 km. The algorithm converged to the following parameter estimates for block IV: $k_z = 0.65 \pm 0.03$ s^{-1}, $k_x = 0.0 \pm 0.01$ s^{-1}, $\epsilon = 0.35 \pm 0.03$ and $\delta = 0.1 \pm 0.02$.

As illustrated by the stacked section in Fig. 5, the boundary between the third and fourth blocks corresponds to a fault that stretches over a significant depth interval. While events in blocks III and IV (i.e. above the dashed line in Fig. 4) are largely flat, and the shallow part of the image in Fig. 5 exhibits good coherence and resolution, most deeper events remain undercorrected.

In contrast to the residual moveout in the first four blocks, the residual moveout in the deeper part of the section (i.e. in block V) noticeably decreases to the right, which indicates a significant lateral velocity variation. To determine the point of velocity continuity at the top of block V in the presence of

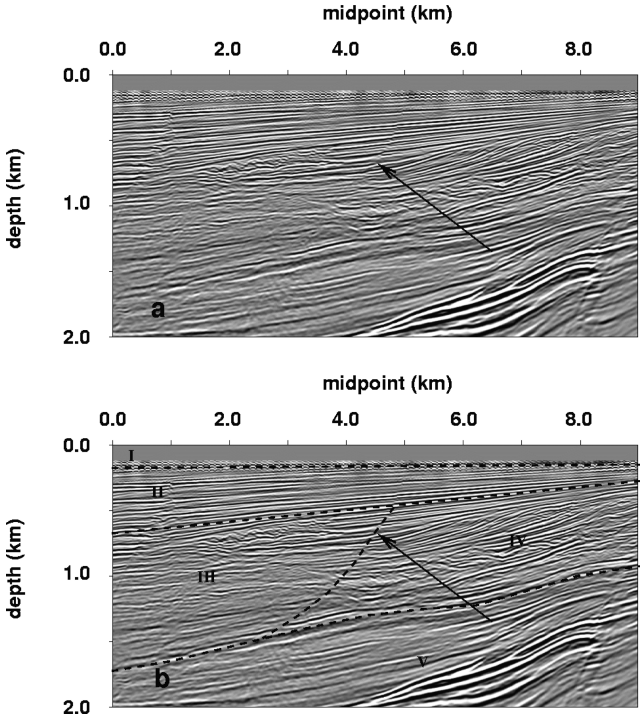

Figure 5 (a) First 2 km of the stacked depth section after prestack depth migration with the estimated parameters in blocks I–IV; (b) the same section with delineated block boundaries. The arrow indicates the fault that separates blocks III and IV.

laterally varying velocity, we followed the procedure outlined in Paper II. First, we performed prestack depth migration for a homogeneous isotropic medium using the vertical velocity at the bottom of block IV ($V_{P0} = 2230$ m/s). Since the minimum residual moveout in block V was observed at midpoint 7 km, the coordinates of the continuity point were found to be $x = 7000$ m, $z = 1235$ m, where $V_{P0} = 2230$ m/s. Although this way of building a continuous velocity function relies on the assumption that the parameter δ is small, it is acceptable for most practical situations (see Paper II).

Using the estimated vertical velocity at the top of block V, we obtained the rest of the parameters from the residual moveout along the two reflectors marked in Fig. 6 for midpoints between 4 km and 6 km: $k_z = 0.83 \pm 0.04$ s^{-1}, $k_x = 0.04 \pm 0.01$ s^{-1}, $\epsilon = 0.19 \pm 0.03$ and $\delta = 0.06 \pm 0.03$. Figures 6 and 7 display the final stacked image obtained after migration with the estimated parameters in all five blocks and the corresponding common-image gathers, most of which are practically flat.

The results of the velocity analysis are summarized in the depth sections of the vertical velocity and parameter η in Figures 8 and 9. As expected, the ubiquitous presence of shales in the subsidence unit at depths less than 2 km makes blocks III and IV strongly anisotropic, with values of η exceeding 0.2. The deeper post-rift unit also exhibits non-negligible anisotropy and is characterized by moderate lateral velocity variation. In the subsidence unit, the maximum offset-to-depth ratio for the two reflectors used in the velocity analysis is close to two, which is large enough to provide sufficiently tight constraints on the parameter η. In the post-rift unit, however, the maximum offset-to-depth ratio is suitable for evaluating η only for the shallow reflector. As a result, estimates of η for depths exceeding 2 km become unstable.

For this line, our maximum values of η exceed 0.2, which is larger than $\eta_{max} \approx 0.1$ obtained by Alkhalifah (1996). Although this discrepancy seems to be quite significant, non-hyperbolic moveout inversion of horizontal events is known to be hampered by the trade-off between η and the NMO velocity. As shown by Grechka and Tsvankin (1998) and Tsvankin (2001), the uncertainty in η estimates for offset-to-depth ratios of about two can reach ± 0.1. This instability in the inversion for η may have influenced our MVA technique and Alkhalifah's time-domain algorithm in different ways, in particular because the model assumptions in the two methods are not the same. Although Alkhalifah (1996) does not take lateral velocity variation into account, his method allows η to vary as a smooth function of the vertical time. In contrast, our MVA algorithm is designed to decouple anisotropy from vertical and lateral heterogeneity, but all anisotropic parameters are held constant within each factorized block.

On the whole, the estimates of η given here are expected to be more precise, both because of the careful treatment of the spatial velocity variations and because of the higher stability of MVA (compared with time-domain techniques) in the presence of noise. The accuracy of our results is confirmed by the close match of the time–depth curve computed from our estimated vertical velocity with borehole data (Fig. 10). We should keep in mind, however, that the MVA method operating solely with P-wave data can reconstruct the vertical velocity in subhorizontal VTI layers only if the assumption about the continuity of V_{P0} across layer boundaries is correct (Paper II).

SECOND LINE

Although migration velocity analysis generally improves parameter estimation because of its robustness in the presence of noise, its main advantage over time-domain methods is in the ability to build laterally varying velocity fields. In this section, the MVA algorithm is applied to another line from the

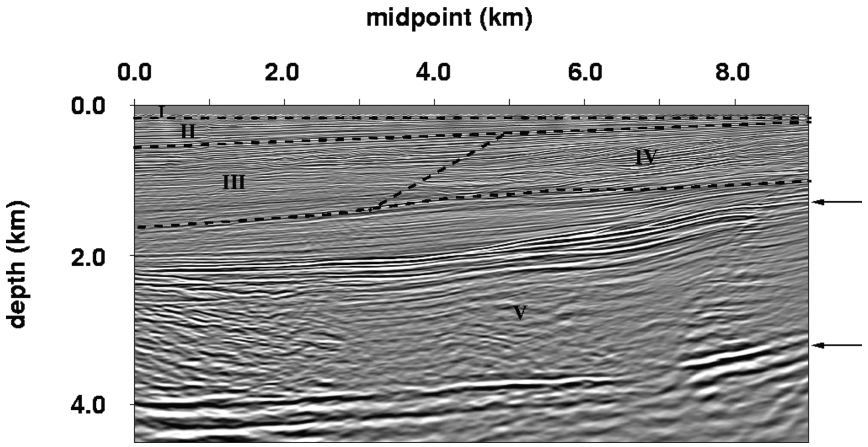

Figure 6 Stacked section after prestack depth migration with the estimated parameters in all five blocks. The arrows mark the events used in the velocity analysis for block V. The first (shallow) marked reflector is the bottom of the subsidence unit, and the second reflector is the bottom of the post-rift unit. Note that the block boundaries of the velocity field do not follow the geological markers.

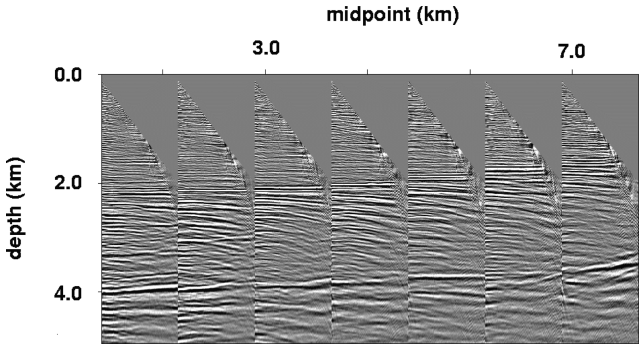

Figure 7 Common-image gathers after prestack depth migration with the estimated parameters. Most undercorrected events stack at extremely low velocities, and are probably interbed multiples.

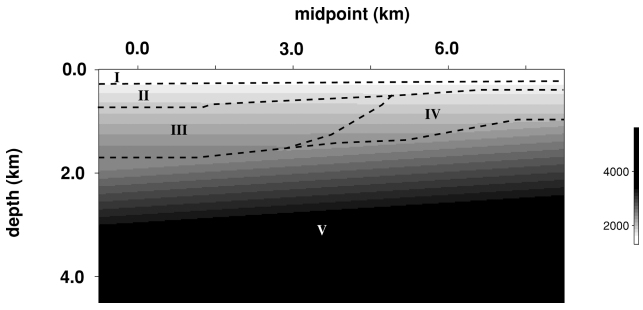

Figure 8 Depth section of the estimated vertical-velocity field. The dashed lines mark the block boundaries. The values in the legend are in m/s.

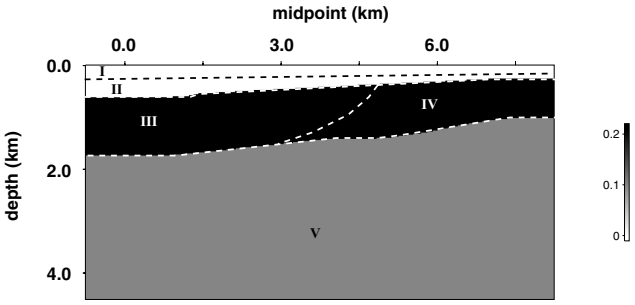

Figure 9 Depth section of the estimated anellipticity parameter η.

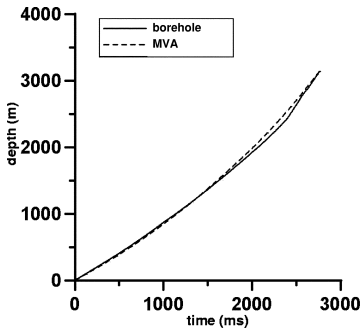

Figure 10 Comparison of the time–depth curves estimated from the MVA at midpoint 5 km (dashed) and derived from sonic logs and check-shot data in a borehole close to the seismic line (solid).

same data set, where the anisotropy parameters and vertical velocity vary significantly in both vertical and horizontal directions. This line is further offshore and has a slightly deeper water column than does the first line. In addition to the same preprocessing steps as those applied to the first line, the data were bandpass-filtered between 5 Hz and 35 Hz.

The final depth-migrated section and the factorized VTI blocks that comprise the model are shown in Fig. 11. The medium parameters in each block (Table 1 and Figs 12–15) were estimated using the same procedure as that applied to the first line. For blocks II, III, IV and V, the MVA was performed with a fixed value of the vertical velocity at the top of each block. We assumed that V_{P0} was continuous between blocks I and II, I and V, II and III, and II and IV. Since the vertical velocity in blocks I, II, III and V is almost laterally invariant,

Table 1 Estimated parameters for the different blocks (second line) that were used to obtain the depth-migrated section shown in Fig. 11. x and z are the continuity points at the top of each block where the listed values of V_{P0} were measured. Block I is isotropic and homogeneous with water velocity of 1500 m/s and is not listed here.

Block	x (km)	z (km)	V_{P0} (m/s)	$k_x(s^{-1})$	$k_z(s^{-1})$	ϵ	δ
II	4	0.24	1500	0.02±0.01	0.66±0.03	0.02±0.02	−0.02±0.02
III	6	0.65	1890	0.01±0.01	0.4±0.04	0.12±0.03	0.03±0.03
IV	2.5	1.4	2200	−0.07±0.02	0.4±0.04	0.19±0.03	0.07±0.03
V	8.5	0.25	1500	0.03±0.02	0.65±0.03	0.15±0.02	0.06±0.02
VI	6.5	1.95	2500	0.16±0.02	0.65±0.03	0.0	0.0

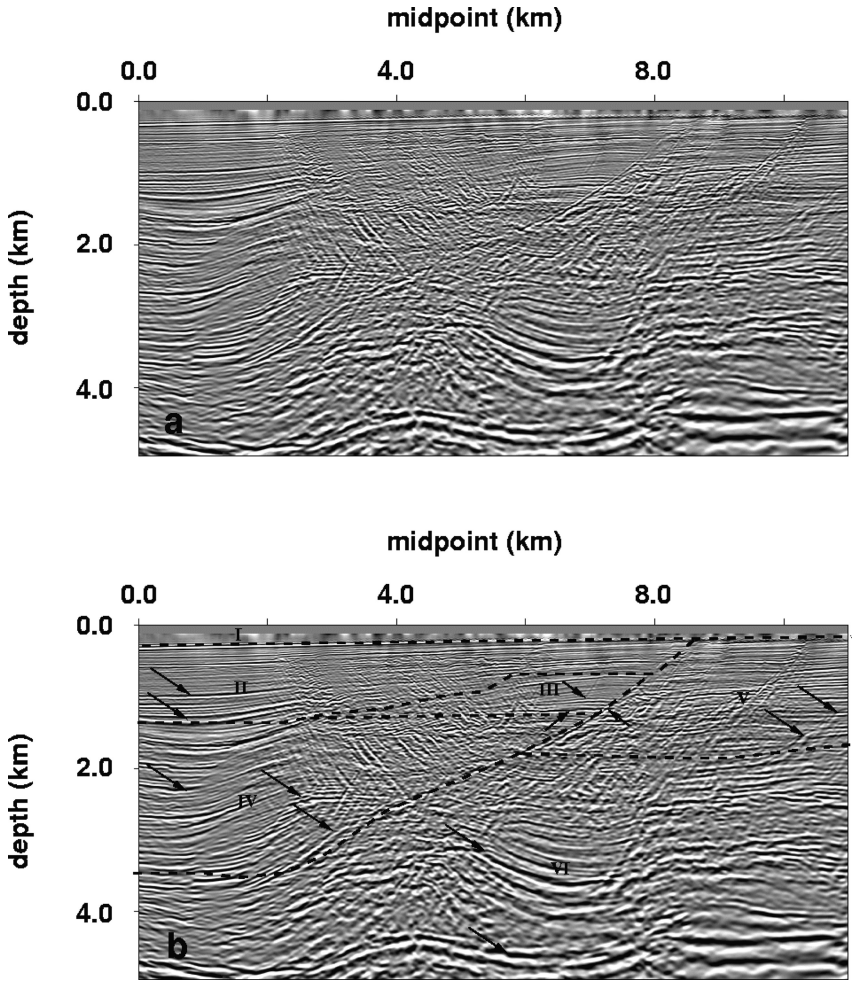

Figure 11 (a) Stacked section for the second line after prestack depth migration with the estimated parameters listed in Table 1; (b) the same section with delineated block boundaries. The arrows indicate the reflectors used in the MVA.

the choice of this point of continuity was not important. For the fourth block, however, the lateral gradient k_x is substantial, and the continuity point was identified by applying the methodology discussed above for the first line.

The maximum offset-to-depth ratio for most reflectors in block IV is less than two, which is insufficient for estimating the parameter η from non-hyperbolic moveout of subhorizontal events. To constrain η, we used reflections from the

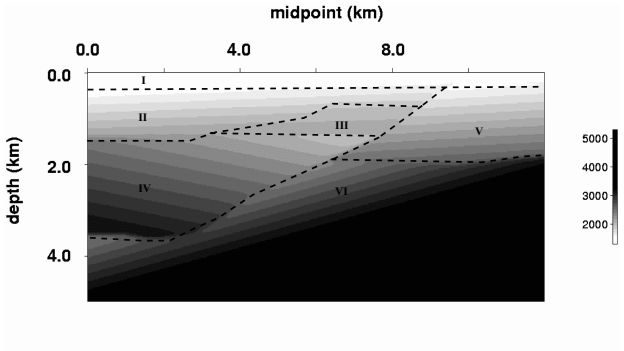

Figure 12 Depth section of the estimated vertical-velocity field for the second line.

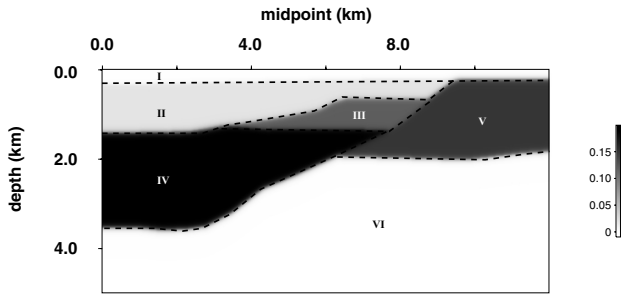

Figure 13 Depth section of the parameter ϵ.

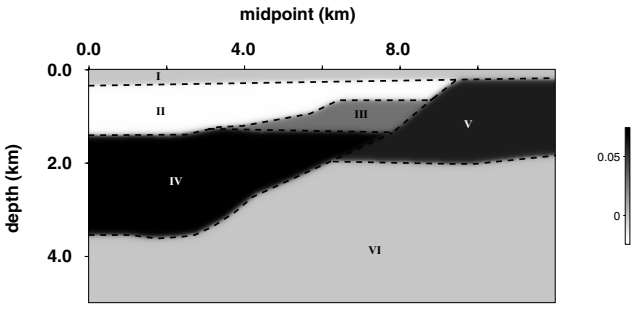

Figure 14 Depth section of the parameter δ.

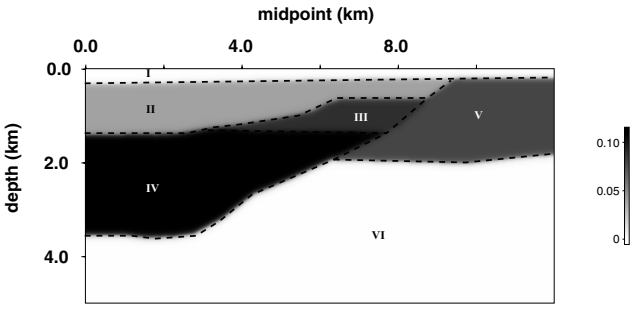

Figure 15 Depth section of the parameter η.

prominent fault plane with a dip of about 35° at the bottom of this block. Reflections from the shallow segment of the same dipping fault plane also provided important information for the parameter estimation in block III.

We had to ignore anisotropy in block VI because η could not be obtained from either non-hyperbolic moveout (the maximum offset-to-depth ratios were close to one) or dipping events. Although a steeply dipping fault plane exists at midpoint 7.5 km and depth 3 km, which may suggest the possibility of estimating the anisotropy from just the hyperbolic component of the moveout, reflections from it were found to be too weak to permit a stable inversion for the parameter η. The velocity V_{P0} at the top of the block and the gradients k_z and k_x were estimated from the hyperbolic portion of the moveout curve for two reflectors sufficiently separated in depth.

The image gathers in Fig. 16 demonstrate that the migration with the estimated model parameters flattens the majority of the reflection events, which confirms that the piecewise-factorized VTI medium is a good approximation for the velocity field in the area. The remaining residual moveout for several events is probably caused by multiples and velocity variations on a scale much smaller than the spread of a typical CMP gather.

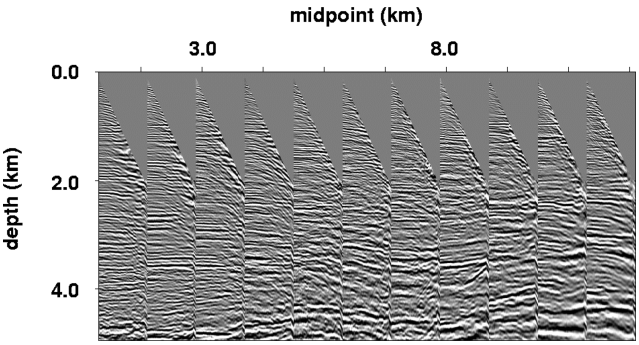

Figure 16 Common-image gathers (at 1-km spacing) after migration with the estimated parameters.

Blocks II, III, IV, V and the portion of block VI above the first prominent reflector make up the subsidence unit, while the deeper part of the section belongs to the post-rift unit. Blocks IV ($k_x = -0.07$ s^{-1}) and VI ($k_x = 0.16$ s^{-1}) exhibit significant lateral velocity variation, which causes a decrease in V_{P0} towards the middle of the section.

The magnitude of the parameter η for this line ($\eta_{max} \approx 0.12 \pm 0.04$) is smaller than that for the first line. One possible reason for the lower η values is the influence of overpressure, which is well documented in this area (Brice *et al.* 1982; Alkhalifah 1996). Existing theoretical and experimental

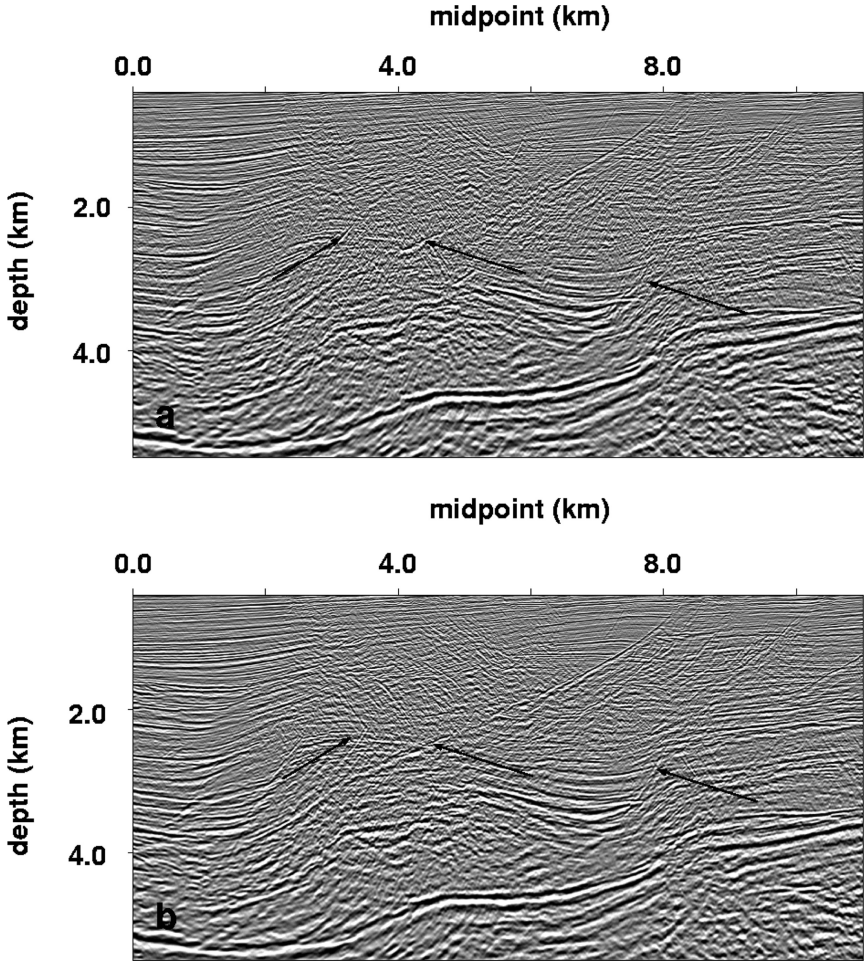

Figure 17 Second section after (a) isotropic and (b) anisotropic time imaging (from Alkhalifah *et al.* 1996). Both sections were filtered to match the amplitude spectrum of the depth-migrated section in Fig. 11 and stretched to depth using the vertical-velocity function from Fig. 12 that was evaluated at midpoint 6 km. The arrows indicate the main improvements achieved by taking anisotropy into account.

studies (e.g. Sarkar *et al.* 2003) show that stress-induced anisotropy tends to be close to elliptical. Also, the shales near the second line may be less consolidated, and the clay platelets responsible for the effective anisotropy may not be well aligned. Although the magnitude of η is substantial only in blocks III, IV and V, geological data indicate that the shales extend all the way to the bottom of the subsidence unit in block VI. Accurate estimation of η in block VI, however, requires larger offsets for subhorizontal events or more prominent dipping events.

Figure 17 was used by Alkhalifah (1996) and Alkhalifah *et al.* (1996) to illustrate the improvements achieved by anisotropic time imaging. For example, the anisotropic processing succeeded in imaging the fault plane at midpoint 7.5 km and depth 3 km (Fig. 17b), which is absent on the isotropic image (Fig. 17a). Also, the major fault plane that runs through the section between midpoints 2 and 8 km and subhorizontal reflectors near midpoint 3 km and depth 2.7 km show improved continuity on the anisotropic section.

Comparison of the anisotropic prestack depth-migrated image in Fig. 18(b) and the time-migrated image in Fig. 18(a) illustrates further improvements achieved by the MVA and prestack depth migration. Better focusing and continuity are observed for the major fault plane between midpoints 2 km and 8 km and several reflectors just above and below it, for the subhorizontal reflectors at midpoint 4.5 km and depth 1.4 km, and for the fault plane at midpoint 7.5 km and depth 3 km. Since time migration ignores the lateral velocity variation in block IV, the antithetic faults, which are clearly visible at midpoint 4 km and depth 2 km on the depth-migrated section, appear fuzzy in Fig. 18(a).

Perhaps the most dramatic difference between the two images is in the shape and position of the two prominent reflectors that define the top and bottom of the post-rift unit (between depths 2.5 km and 5 km) and span the entire lateral extent of the section. Because time migration does not account for the lateral variation in the vertical velocity, these two reflectors appear dipping on the time-migrated image. This dip

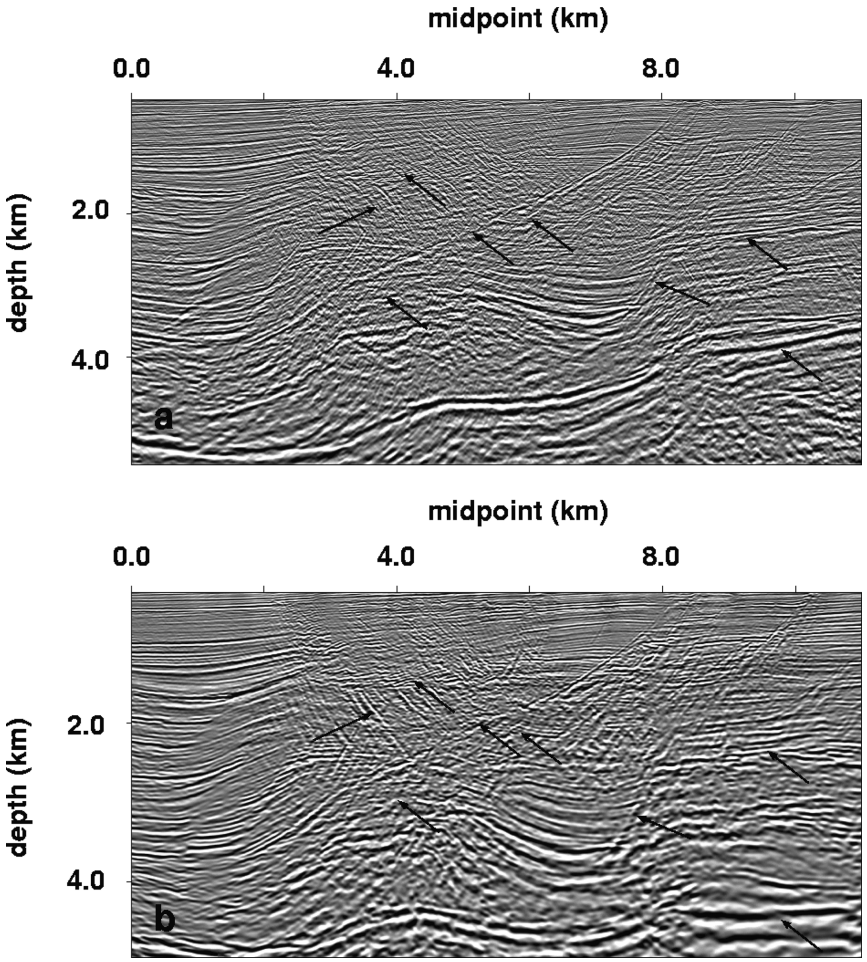

Figure 18 Second section after (a) anisotropic time imaging (Fig. 17b) and (b) anisotropic prestack depth migration (Fig. 11). The arrows indicate the main improvements achieved by applying the MVA and prestack depth migration.

was largely removed in Fig. 18(b) by taking into account the significant lateral velocity variation in block VI.

As was the case for the first line, our estimates of the maximum value of η ($\eta_{max} \approx 0.12$) are somewhat different from those reported by Alkhalifah (1996) and Alkhalifah *et al.* (1996) ($\eta_{max} \approx 0.2$). We believe that the main reason for this discrepancy is the presence of significant lateral heterogeneity in blocks IV and VI, which was not taken into account in the DMO-based inversion method of Alkhalifah (1996). The high image quality in Fig. 18(b) indicates that the application of our MVA method helped to describe the spatially varying anisotropic velocity field with greater resolution and accuracy compared to those for the time-domain techniques.

DISCUSSION AND CONCLUSIONS

By approximating the subsurface with factorized $v(x, z)$ VTI media, it is possible to account properly for both vertical and lateral variation in the anisotropic velocity field. Here, we applied to field data a migration velocity-analysis method designed for VTI models composed of factorized blocks or layers. This MVA algorithm, introduced by Sarkar and Tsvankin (2004; Paper II) has two important new features that distinguish it from conventional velocity-analysis techniques:

1 Since estimation of the anisotropic coefficient η often requires non-hyperbolic (long-spread) moveout information, we implemented a two-parameter semblance scan on image gathers to evaluate both hyperbolic and non-hyperbolic parts of the residual moveout function. When the semblance operator fails because of substantial amplitude variation with offset, as may occur in the presence of polarity reversals in Class II sands, modified semblance routines suggested by Sarkar *et al.* (2001) and Sarkar *et al.* (2002) may be used instead.

2 Evaluation of the vertical and lateral velocity gradients in each block is accomplished by minimizing residual moveout along at least two reflectors sufficiently separated in depth.

Application of our MVA method to offshore data from West Africa confirms the results of previous studies (Ball 1995; Alkhalifah 1996; Alkhalifah *et al.* 1996; Toldi *et al.* 1999) that massive shales in that area are strongly anisotropic, with the parameter η on one of the lines exceeding 0.2. The reconstructed velocity field also indicates the presence of substantial lateral heterogeneity in some of the layers, which was unaccounted for by the time-domain techniques of Alkhalifah *et al.* (1996) and Toldi *et al.* (1999). Since the piecewise-factorized VTI model can handle both anisotropy and heterogeneity, our MVA algorithm produced more accurate estimates of the anisotropic coefficients than those obtained previously in the time domain.

Anisotropic prestack depth migration with the reconstructed velocity field resulted in a number of significant improvements in image quality compared to the anisotropic time sections (Alkhalifah *et al.* 1996). In particular, most faults on the depth-migrated image show greater continuity, the antithetic faults that are fuzzy on the time images are well focused, and subhorizontal reflectors within the anisotropic layers are better positioned and stacked. The depth imaging substantially changed the structure of the deeper part of one of the sections, where false dips seen on the time-migrated image were removed after the MVA and prestack depth migration.

Flat image gathers after the iterative migration velocity analysis suggest that the model composed of factorized $v(x, z)$ VTI blocks provides an adequate approximation for realistic, spatially varying, anisotropic velocity fields. Although the vertical velocity can seldom be constrained by P-wave reflection data alone, the field-data example discussed here indicates that the assumption of a continuous vertical velocity field offers a practical way to build anisotropic models for prestack depth migration with minimal *a priori* information. Furthermore, as confirmed by this case study, in the absence of pronounced velocity jumps across medium interfaces, the time–depth curve obtained from the MVA algorithm closely matches the curve computed from borehole data.

Similar to any other MVA technique, the main cost of our method is in the repeated application of prestack migration, which makes this algorithm substantially more expensive than the time-domain parameter-estimation methods of Alkhalifah and Tsvankin (1995), Alkhalifah *et al.* (1996) and Grechka *et al.* (2002). The time-domain algorithms, however, produce inferior results in the presence of lateral velocity variation, as illustrated by the examples above.

Although the need to use anisotropic ray tracing makes our migration algorithm more time-consuming than the conventional isotropic techniques, this extra cost is insignificant in comparison with the computing time for the actual migration step, which does not change for anisotropic media. However, because of the larger number of medium parameters, including anisotropy in MVA leads to a slower convergence towards the best-fit model.

ACKNOWLEDGMENTS

We are grateful to Greg Ball and John Toldi of ChevronTexaco for numerous helpful suggestions and for making the data available to CWP. We thank members of the A(nisotropy)-Team of the Center for Wave Phenomena (CWP), Colorado School of Mines, for useful discussions and Ken Larner (CSM) and the referees of *Geophysical Prospecting* for their reviews of the manuscript. The support for this work was provided by the Consortium Project on Seismic Inverse Methods for Complex Structures at CWP and by the Chemical Sciences, Geosciences and Biosciences Division, Office of Basic Energy Sciences, Office of Science, U.S. Department of Energy.

REFERENCES

Alkhalifah T. 1996. *Velocity analysis for transversely isotropic media*. PhD Thesis, Colorado School of Mines.

Alkhalifah T. 1997. Velocity analysis using nonhyperbolic moveout in transversely isotropic media. *Geophysics* **62**, 1839–1854.

Alkhalifah T. and Tsvankin I. 1995. Velocity analysis for transversely isotropic media. *Geophysics* **60**, 1550–1566.

Alkhalifah T., Tsvankin I., Larner K. and Toldi J. 1996. Velocity analysis and imaging in transversely isotropic media: Methodology and a case study. *The Leading Edge* **15**, 371–378.

Ball G. 1995. Estimation of anisotropy and anisotropic 3-D prestack migration, offshore Zaire. *Geophysics* **60**, 1495–1513.

Brice S.R., Cochran M.D., Pardo G. and Edwards A.D. 1982. Tectonics and sedimentation of the South Atlantic rift sequence: Cabinda, Angola. In: *Studies in Continental Margin Geology*, Vol. 34 (eds J.S. Watkins and C.L. Drake), pp. 5–18. AAPG memoir.

Chauris H. and Noble M. 2001. Two-dimensional velocity macro model estimation from seismic reflection data by local differential semblance optimization: Application to synthetic and real datasets. *Geophysical Journal International* **144**, 14–26.

Faust L.Y. 1953. A velocity function including lithologic variation. *Geophysics* **18**, 271–288.

Gardner G.H.F., French W.S. and Matzuk T. 1974. Elements of migration and velocity analysis. *Geophysics* **39**, 811–825.

Grechka V., Pech A. and Tsvankin I. 2002. P-wave stacking-velocity tomography for VTI media. *Geophysical Prospecting* **50**, 151–168.

Grechka V. and Tsvankin I. 1998. Feasibility of nonhyperbolic moveout inversion in transversely isotropic media. *Geophysics* **63**, 957–969.

Han B., Galikeev T., Grechka V., Le Rousseau J. and Tsvankin I. 2000. A synthetic example of anisotropic P-wave processing for a model from the Gulf of Mexico. In: *Anisotropy 2000: Fractures, Converted Waves and Case Studies* (eds L. Ikelle and A. Gangi), pp. 311–325. Society of Exploration Geophysicists.

Liu Z. 1997. An analytical approach to migration velocity analysis. *Geophysics* **62**, 1238–1249.

Meng Z. 1999. *Tetrahedral based earth models, ray tracing in tetrahedral models and analytical migration velocity analysis*. PhD Thesis, Colorado School of Mines, Dept. of Geophysics, Golden, Colorado, USA.

Sarkar D., Bakulin A. and Kranz R.L. 2003. Anisotropic inversion of seismic data for stressed media: Theory and a physical modeling study on Berea Sandstone. *Geophysics* **68**, 690–704.

Sarkar D., Baumel R.T. and Larner K. 2002. Velocity analysis in the presence of amplitude variation. *Geophysics* **67**, 1664–1672.

Sarkar D., Castagna J.P. and Lamb W. 2001. AVO and velocity analysis. *Geophysics* **66**, 1284–1294.

Sarkar D. and Tsvankin I. 2003. Analysis of image gathers in factorized VTI media. *Geophysics* **68**, 2016–2025.

Sarkar D. and Tsvankin I. 2004. Migration velocity analysis in factorized VTI media. *Geophysics* **69**, 708–718.

Sexton P. and Williamson P. 1998. 3D anisotropic velocity estimation by model based inversion of prestack traveltimes. 68th SEG Meeting, New Orleans, USA, Expanded Abstracts, 1855–1858.

Stork C. 1988. *Raytrace tomographic velocity analysis of surface seismic reflection data*. PhD Thesis, California Institute of Technology, Pasadena, California, USA.

Stork C. 1992. Reflection tomography in the post-migrated domain. *Geophysics* **57**, 680–692.

Taner M.T. and Koehler T. 1969. Velocity spectra: Digital computer derivation and application of velocity functions. *Geophysics* **34**, 859–881.

Thomsen L. 1986. Weak elastic anisotropy. *Geophysics* **51**, 1954–1966.

Toldi J., Alkhalifah T., Berthet P., Arnaud J., Williamson P. and Conche B. 1999. Case study of estimation of anisotropy. *The Leading Edge* **18**, 588–594.

Tsvankin I. 2001. *Seismic Signatures and Analysis of Reflection Data in Anisotropic Media*. Elsevier Science Publishing Co.

Williamson P., Berthet P., Mispel J. and Sexton P. 1999. Anisotropic velocity model construction and migration: An example from West Africa. 69th SEG Meeting, Houston, USA, Expanded Abstracts, 1592–1595.

APPENDIX

MVA in the presence of non-linear velocity variation

The purpose of this appendix is to evaluate the distortions produced by our MVA algorithm when the vertical velocity is a *non-linear* function of depth z. Consider a factorized VTI medium with the vertical velocity defined as $V_{P0}(z) = V_{P0} + A z^2$, and assume that reflection moveout was recorded from eight horizontal interfaces at depth intervals of 500 m.

To reconstruct the vertical velocity variation, we approximated the subsurface with the three horizontal factorized $v(z)$ layers marked in Fig. 19(a). Using the moveout associated with two reflectors for each factorized $v(z)$ layer, we obtained a piecewise-factorized medium with the function $V_{P0}(z)$

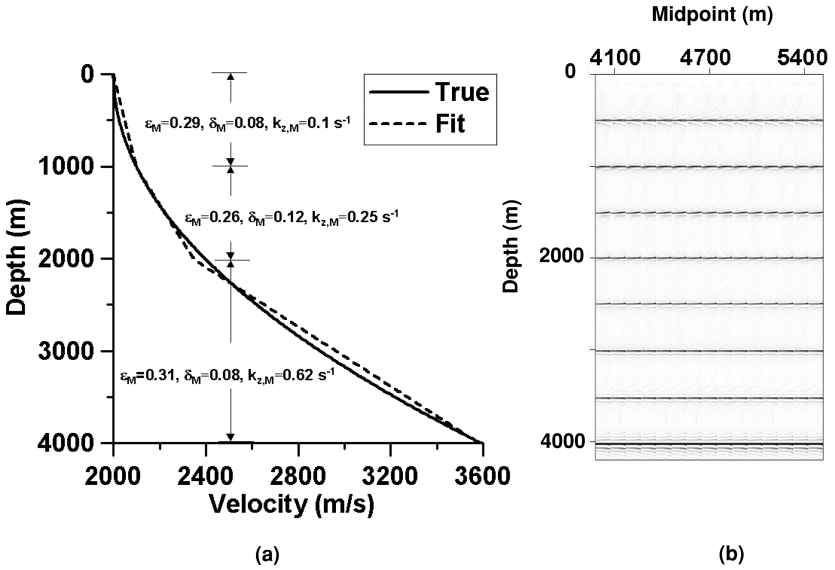

Figure 19 (a) Comparison of the true (solid line) and estimated (dashed line) vertical velocity V_{P0} for a VTI medium with $V_{P0}(z) = 2000 + 0.0001z^2$ (z is in metres, V_{P0} is in m/s), $\epsilon = 0.3$ and $\delta = 0.1$. The migration velocity analysis was performed for three factorized $v(z)$ layers with the boundaries marked on the plot. The reflectors are spaced every 500 m, and the maximum offset is equal to 4000 m. The interval parameters (subscript M) were estimated using the moveout associated with two reflectors in each factorized layer. (b) Image gathers obtained after prestack depth migration with the estimated parameters shown on plot (a).

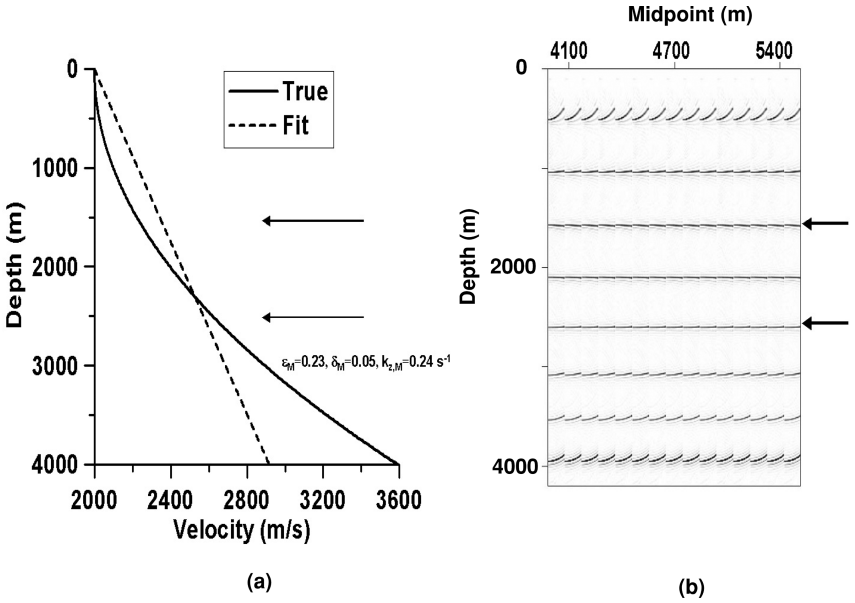

Figure 20 Same as Fig. 19, but the MVA was performed for a single factorized $v(z)$ layer using the moveout associated with the reflectors at depths 1500 and 2500 m (marked by the arrows).

that closely reproduces the true non-linear vertical-velocity variation (Fig. 19a). The vertical velocity at the top of the model was fixed at the correct value, while the velocities in the two deeper layers were found under the assumption that V_{P0} is a continuous function of depth. The accuracy of the estimated three-layer factorized model is confirmed by the flat image gathers in Fig. 19(b).

The success of the piecewise-linear velocity approximation, however, depends on whether the available reflectors sample the velocity function in sufficient detail. Consider the same true medium as that in Fig. 19, but now with only two reflectors (located at depths of 1500 m and 2500 m) available for velocity analysis. In this case, our MVA algorithm can estimate the parameters of just one factorized $v(z)$ layer (Fig. 20a). As illustrated by the image gathers in Fig. 20(b), the events associated with the reflectors used in the velocity analysis are flat. Events both above 1500 m and below 2500 m, however, are overcorrected because the NMO velocities for them are too low. Clearly, no single factorized medium can properly image reflection events for the whole range of depths.